SAR Image Despeckling by the Use of Variational Methods With Adaptive Nonlocal Functionals

Xiaoshuang Ma, Huanfeng Shen, *Senior Member, IEEE*, Xile Zhao, and Liangpei Zhang, *Senior Member, IEEE*

***Abstract*—In this paper, we focus on the despeckling of synthetic aperture radar (SAR) images by variational methods which introduce nonlocal regularization functionals. To achieve this goal, two models are investigated from different aspects. The first model is derived for the logarithmically transformed (homomorphic) domain of the SAR data, and the other is derived for the original (nonhomomorphic) domain. The statistical properties of the speckle and the log-transformed speckle are analyzed, and the similarity measurements between pixels in the homomorphic domain and nonhomomorphic domain are then derived for constructing the corresponding nonlocal regularization functionals. Meanwhile, in the proposed models, we develop a strategy to adaptively choose the regularization parameters based on both the local heterogeneity information and the noise level of the images, aiming at getting a better balance between the goodness of fit of the original data and the amount of smoothing. A quasi-Newton iteration method is employed to quickly minimize the proposed adaptive nonlocal functionals. Experiments conducted on both simulated images and real SAR images confirm the good performances of the proposed methods, both in reducing speckle and preserving image quality.**

***Index Terms*—Homomorphic filter, nonlocal functional, speckle, variational method.**

I. INTRODUCTION

IT IS well known that synthetic aperture radar (SAR) images are inherently affected by speckle noise, which is due to the coherent interference of waves reflected from many elementary scatterers. Speckle noise has long been recognized as one of the most crucial problems of SAR data. The presence of speckle complicates the image interpretation and analysis and reduces the effectiveness of target detection and classification [1], [2]. Despeckling can therefore be an essential procedure before using SAR images to obtain land-cover information.

An alternative method of reducing speckle is the multilook process, which amounts to incoherently averaging a certain number (defined by the number of looks) of independent images, thus reducing the noise intensity, but at the cost of a clear loss in spatial resolution. Therefore, to significantly reduce speckle and, at the same time, to effectively preserve the scene features, filtering techniques are necessary. In the early years, speckle reduction techniques were often operated in the spatial domain with linear filters based on a minimum mean-square error (MMSE) approach, e.g., the Lee filter [3], Kuan filter [4], sigma filter [5], and their refined versions [6], [7]. Some other early methods use the so-called homomorphic approach [8], [9], taking the log of the data so as to obtain a more tractable additive model and then applying certain well-known methods drawn from the additive white Gaussian noise (AWGN) denoising literature. These conditional low-pass filters have high processing efficiency but show limitations in either preserving image sharpness or effectively suppressing speckle. In the recent decades, some new filter-based methodologies have been presented and have been successful in SAR image despeckling. Two typical categories of these algorithms are the nonlocal filters [10]–[13] and the wavelet-based filters [14]–[16]. A detailed introduction to the current research situation for SAR despeckling can be found in [17] and [18].

In addition to the filter-based techniques in the spatial domain and in the frequency domain, the variational methods are another important branch of image denoising, which break through the traditional idea of filters by solving the problem of energy optimization. In the framework of the variational methods, image denoising problems are considered as variational problems, where a clean image is obtained by minimizing an energy functional. Such functionals often consist of a fidelity term, such as the norm of the difference between the clean image and the original noisy image, and a regularization term, which includes prior information about the original image. In 1992, Rudin *et al.* [19] innovatively introduced the variation regularization approach for AWGN denoising (the ROF model), and this approach has since raised wide research interest in image processing and computer vision [20], [21]. In the last few years, a number of variational models have also been developed for removing multiplicative noise (including speckle). Following the maximum *a posteriori* (MAP) estimator for multiplicative gamma noise, Aubert and Aujol [22] introduced a nonconvex model (AA model), whose data term was subsequently adopted in a convex model by Shi and Osher in [23] (the SO model). The model of Shi and Osher was modified in [24] by adding a quadratic term to obtain a simpler alternating minimization algorithm. Steidl and Teuber [25]

Manuscript received October 2, 2014; revised March 21, 2015, October 8, 2015, and December 3, 2015; accepted January 9, 2016. This work was supported in part by the National Natural Science Foundation of China under Grants 41271376 and 41422108 and in part by the Program for Changjiang Scholars and Innovative Research Team in University (IRT1278). *(Corresponding author: Huanfeng Shen.)*

X. Ma is with the Department of Resource and Environmental Sciences, Wuhan University, Wuhan 430079, China (e-mail: mxs.88@whu.edu.cn).

H. Shen is with the School of Resource and Environmental Sciences, Wuhan University, Wuhan 430079, China, the Key Laboratory of Geographic Information System, Ministry of Education, Wuhan University, Wuhan 430079, China, and also with the Collaborative Innovation Center of Geospatial Technology, Wuhan University, Wuhan 430079, China (e-mail: shenhf@whu.edu.cn).

X. Zhao is with the University of Electronic Science and Technology of China, Chengdu 610051, China (e-mail: xlzhao122003@163.com).

L. Zhang is with the State Key Laboratory of Information Engineering in Surveying, Mapping and Remote Sensing, Wuhan University, Wuhan 430079, China (e-mail: zlp62@whu.edu.cn).

Color versions of one or more of the figures in this paper are available online at http://ieeexplore.ieee.org.

Digital Object Identifier 10.1109/TGRS.2016.2517627

studied a variational model consisting of Kullback–Leibler divergence as the data-fitting term and total variation as the regularization term. Recently, Teuber *et al.* [26] have studied the problem of removing multiplicative noise by using seminorm regularization models with I-divergence constraints, and this approach can realize the task of removing both Poisson noise and gamma noise by estimating the constraining parameter based on the type of noise. Yun and Woo [27] have proposed using the mth root transformation to deal with the nonconvexity of the AA model. Zhao *et al.* [28] have proposed a new convex optimization model for multiplicative noise and blur removal.

Although most variational methods can obtain positive results in suppressing speckle, the drawbacks of the staircase effect and the smearing of the image features degrade their despeckling performances. In addition, the regularization term of the conventional variational methods only considers local prior information, which might also lead to undesirable despeckling results in some cases. In this paper, we focus on the despeckling of SAR images by variational methods. In contrast to most of the well-known variational methods, we investigate two models which involve nonlocal regularization functionals. The main motivation behind such nonlocal regularization models comes from the work of Gilboa *et al.* [29] and Lou *et al.* [30], who used nonlocal functionals for the denoising and recovery of AWGN-contaminated images. One of our proposed models is derived for the logarithmic domain of the SAR data, and the other is derived for the original domain. In the proposed nonlocal functionals, the regularization parameters are adaptively tuned based on the local heterogeneity information and the noise level of the images. As for the rapid implementation of the proposed adaptive nonlocal functional (ANLF) models, we adopt a quasi-Newton iteration method.

The remainder of this paper is organized as follows. We start by reviewing some classical energy methods for denoising in Section II. In Section III, the statistical properties of speckle and logarithmically transformed speckle are analyzed, and the two ANLF models are presented. In Section IV, the implementation of the proposed ANLF models is described. Finally, we demonstrate the performances of the proposed algorithms in Section V and give our conclusion in Section VI.

II. Brief Introduction to some Classical Variational Denoising Models

A. Variational Models for AWGN-Contaminated Images

1) ROF Model: A variational method aims to restore the original image by finding the minimum of some appropriate functional in the space $\Omega \subset R^2$, which is connected and bounded. Rudin *et al.* [19] first employed this method for the removal of AWGN by minimizing the following functional:

$$J(u) = \int_\Omega |\nabla u| dx + \lambda \int_\Omega (f-u)^2 dx \tag{1}$$

where ∇ is the gradient operator. The first term of the right-hand side of the aforementioned functional denotes the *regularization term*, which includes prior information about the noise-free image u, and the second term denotes the *data-fitting term* (fidelity term), which depends on the given (corrupted) data f. $\lambda > 0$ is a regularization parameter to control the tradeoff between the goodness of fit of f and a smoothing requirement due to the regularization term.

2) Nonlocal Functional Models: The conventional variational models have many desirable properties. However, their main drawbacks consist of their staircase effect and the regularization term that only takes into account the local information. Various alternative regularization terms have been considered to solve this problem. Among them, the nonlocal regularization term leads to very good denoising results by replacing the classical regularization term with a nonlocal functional. The idea of nonlocal means (NL_means) goes back to [31], and it was incorporated into the variational framework in [29] and [30]. For the denoising or recovery of images contaminated by AWGN, a difference-based nonlocal functional can be formulated as

$$J(u) = \int_\Omega \psi \left[(u(x)-u(y))^2 \, w(x,y) \right] dydx + \lambda \int_\Omega (f-u)^2 dx \tag{2}$$

where $(u(x)-u(y))^2$ can be regarded as prior information about the difference between two pixels contaminated by AWGN; $w(x,y) = \exp[-((v(x)-v(y))/h)^2]$ is a weight function, which is constructed using the preprocessed image v as the reference; and h is a scalar parameter. As an example, for total variation (TV), $\psi(\alpha) = \sqrt{\alpha}$, and (2) becomes

$$J_{\frac{NL}{TV}}(u) = \int_\Omega \sqrt{(u(x)-u(y))^2 \, w(x,y) dydx} + \lambda \int_\Omega (f-u)^2 dx. \tag{3}$$

Meanwhile, when $\psi(\alpha) = \alpha$, (2) becomes

$$J_{\frac{NL}{H^1}}(u) = \int_\Omega (u(x)-u(y))^2 \, w(x,y) dydx + \lambda \int_\Omega (f-u)^2 dx. \tag{4}$$

The functional in (4) is analogous to the standard H^1 seminorm, so it is denoted as NL/H^1. The functional in (3) is similarly denoted as NL/TV. Recently, Chierchia *et al.* [32] have extended the NLTV-based regularization by combining it with a structure tensor to recover hyperspectral images which are degraded by blurring and AWGN noise arising from sensor imprecision or physical limitations.

B. Variational Models for Speckled Images

1) AA Model: The ROF model is effective for AWGN denoising, but it performs poorly when removing speckle noise. This is because the data-fitting term in the ROF model is not suitable for gamma-distributed multiplicative noise. Under the hypothesis of fully developed speckle, the observed backscattered intensity of SAR systems can be expressed as

$$f = un \tag{5}$$

where u is the noise-free reflection and n is the speckle noise. It is well known that the speckle of a multilook SAR intensity image can be modeled by a gamma distribution. When dealing with this kind of multiplicative noise, Aubert and Aujol [22] proposed to determine the denoised image by minimizing the following functional:

$$J(u) = \int_\Omega |\nabla u| dx + \lambda \int_\Omega \left(\frac{f}{u} + \log u \right) dx. \tag{6}$$

In the AA model, the data-fitting term follows canonically from the MAP approach related to multiplicative gamma noise. However, some studies [25] have shown that the regularization term is inappropriate, which often leads to the problem of the noise surviving much longer at low image values, and $|\nabla \log u|$ is a better choice.

2) SO Model: To solve the problem that the AA model encounters, Shi and Osher [23] suggested keeping the data-fitting term in (6) and replacing the regular $|\nabla u|$ by $|\nabla \log u|$. Furthermore, setting $E = \log u$. This results in the following variational model:

$$\begin{aligned} \hat{E} &= \arg\min \left\{ \int_\Omega |\nabla E| dx + \lambda \int_\Omega (f e^{-E} + E) dx \right\} \\ \hat{u} &= \exp(\hat{E}). \end{aligned} \tag{7}$$

III. Proposed ANLF Models for SAR Despeckling

A. Homomorphic and Nonhomomorphic Nonlocal Functionals

As described in Section II, the AA model is derived for the original data domain, while the SO model is derived for the logarithmically scaled data domain. They have the same data-fitting terms but different regularization terms. Although the SO model often achieves better performances than the AA model due to the improvement in the regularization term, its ability to preserve image features can still be unsatisfactory in some cases, as revealed in a number of studies [24], [25]. In this paper, we investigate two energy models with nonlocal functionals for the reduction of speckle in SAR intensity images. The data-fitting terms of the proposed nonlocal variational models are the same as those of the AA model and the SO model, respectively, while the classical regularization terms are replaced by nonlocal regularization terms (in this study, we focus on NL/H^1 regularizers for both models, and the NL/TV regularizers are not in the scope of this paper). This results in the proposed nonhomomorphic nonlocal functional model

$$\begin{aligned} J_1(u) &= \lambda \int_\Omega \left(\frac{f}{u} + \log u \right) dx + \int_\Omega \Phi_1(u(x), u(y)) w_1(x,y) dy dx \\ \hat{u} &= \arg\min \{ J_1(u) \} \end{aligned} \tag{8}$$

and the proposed homomorphic nonlocal functional model

$$\begin{aligned} J_2(E) &= \lambda \int_\Omega (f e^{-E} + E) dx + \int_\Omega \Phi_2(E(x), E(y))\, w_2(x,y) dy dx \\ \hat{E} &= \arg\min \{ J_2(E) \} \\ \hat{u} &= \exp(\hat{E}) \end{aligned} \tag{9}$$

where E denotes the logarithmically scaled image of u. $\Phi_1(u(x), u(y))$ and $\Phi_2(E(x), E(y))$ represent the prior similarity information between two pixels in the original data domain and the log-transformed data domain, respectively. $w_1(x,y)$ and $w_2(x,y)$ are the corresponding weights.

Clearly, in the proposed nonlocal functionals, the choice of the prior similarity measurement $\Phi(\cdot)$ between two pixels directly determines the performance of the despeckling. In the AWGN setting, a smaller Euclidean distance corresponds to a higher likelihood that the two signal pixels (without noise) are equal; however, in the non-AWGN setting, the Euclidean distance may lose its significance in measuring the similarity between pixels. In the following section, we briefly recall the statistical properties of speckle and log-transformed speckle and describe the similarity measurements used in the two cases.

B. Statistical Properties of Speckle and the Log-Transformed Speckle

1) Statistical Properties of Speckle and the Nonhomomorphic Nonlocal Functional: To measure the similarity of pixels in the original SAR data domain, we employ the method proposed by Deledalle *et al.* [10]. For the amplitude format of SAR data, it can be modeled as independent and identically distributed, according to the following Nakagami–Rayleigh distribution:

$$p(A|s) = \frac{2}{\Gamma(L)} \left(\frac{L}{s} \right)^L A^{2L-1} \exp\left(-L \frac{A^2}{s} \right), \; A \geq 0 \tag{10}$$

where A is the amplitude, L is the number of looks, and s is the underlying reflection image. $\Gamma(\cdot)$ denotes the gamma function. Mathematically, given two observed amplitude values $A(x)$ and $A(y)$, their similarity measure is related to the probability $p[s(x) = s(y)|A(x), A(y)]$. The larger the probability, the smaller the similarity measure. In a Bayesian framework, without knowledge of $p[s(x) = s(y)]$ and $p[A(x), A(y)]$, the probability $p[s(x) = s(y)|A(x), A(y)]$ is proportional to the likelihood $p[A(x), A(y)|s(x) = s(y)]$, which is

$$\begin{aligned} &p\left[A(x), A(y)|s(x) = s(y)\right] \\ &\quad = \int_D p\left[A(x)|s(x) = a\right] \cdot p\left[A(y)|s(y) = a\right] \cdot p(a) da \end{aligned} \tag{11}$$

where $p(\cdot)$ represents the probability density function. If we assume that, lacking any prior knowledge, $p(\cdot)$ is uniform over the domain D, then considering (10), (11) can be further read as

$$\begin{aligned} p\left[A(x), A(y)|s(x) = s(y)\right] &\propto \int_0^\infty \frac{4L^{2L}}{\Gamma^2(L) a^{2L}} \left[A(x)A(y)\right]^{2L-1} \\ &\quad \times \exp\left\{ -\frac{L}{a} \left[A^2(x) + A^2(y)\right] \right\} da \end{aligned} \tag{12}$$

with the integral equal to

$$4L \frac{\Gamma(2L-1)}{\Gamma^2(L)} \left[\frac{A(x)A(y)}{A^2(x) + A^2(y)} \right]^{2L-1}. \tag{13}$$

Finally, taking the negative logarithm of (13) and discarding the constant terms, the similarity measure is derived as

$$d\left(A(x), A(y)\right) = \log\left(\frac{A^2(x) + A^2(y)}{A(x)A(y)}\right). \tag{14}$$

Note that the similarity measure in (14) is in terms of the amplitude format, and it is symmetrically invariant; hence, the nonhomomorphic nonlocal functional model in (8) for the intensity format can be finally defined as

$$\begin{aligned} J_1 =& \lambda \int\limits_{\Omega} \left(\frac{f}{u} + \log u\right) dx \\ &+ \int\limits_{\Omega} \log\frac{u(x)+u(y)}{\sqrt{u(x)u(y)}} \exp\left\{-\left[\frac{\log\frac{v_1(x)+v_1(y)}{\sqrt{v_1(x)v_1(y)}}}{h}\right]^2\right\} dydx \\ \hat{u} =& \arg\min\left\{J_1(u)\right\} \end{aligned} \tag{15}$$

where v_1 denotes the preprocessed image, which is discussed in the next section, and h is a scalar parameter.

2) Statistical Properties of the Log-Transformed Speckle and the Homomorphic Nonlocal Functional: Speckle in SAR images is modeled as multiplicative random noise, whereas most available filtering algorithms were developed for AWGN in the context of image denoising and restoration, as additive noise is the most common noise type in imaging and sensing systems. To take advantage of these algorithms, homomorphic transformation is often used to convert the multiplicative model into an additive model, with the assumption that the logarithmic SAR image is Gaussian distributed. In fact, it has been found that the logarithmically transformed speckle follows a Fisher–Tippett distribution [33], which can be approximately fitted by a Gaussian distribution when the number of looks of the image is large enough. In our proposed homomorphic nonlocal functional, the Euclidean distance is employed to measure the similarity between two logarithmically scaled pixels, with the assumption of a Gaussian distribution.

One important issue related to the logarithmic transformation that should be pointed out is that the mean of the log-transformed speckle noise is not zero, whereas a significant set of techniques assumes it to be Gaussian white noise with zero mean. For the purpose of radiometric preservation, it is necessary to correct the biased mean within the processing stages, especially for SAR images with high noise levels. In conclusion, the proposed homomorphic nonlocal functional model in (9) is finally modified as

$$\begin{aligned} J_2 =& \lambda \int\limits_{\Omega} (fe^{-E} + E) dx \\ &+ \int\limits_{\Omega} \left(E(x) - E(y)\right)^2 \exp\left(-\left[\frac{v_2(x) - v_2(y)}{h}\right]^2\right) dydx \\ \hat{E} =& \arg\min\left\{J_2(E)\right\} \\ \hat{u} =& \exp(\hat{E} - M) \end{aligned} \tag{16}$$

where M is the mean of the log-transformed speckle, which was found to be a constant value related to the number of looks [33], and v_2 is the preprocessed log-transformed image.

The second terms of J_1 and J_2 are the fidelity terms which measure the difference between the clean image and the original noisy image, and the difference between the clean log-transformed image and the noisy log-transformed image, respectively. These terms ensure that the structures and details in the images can be effectively retained after despeckling. The first terms of J_1 and J_2 are the nonlocal regularization terms for the original image and the transformed image, respectively. These terms play the roles of despeckling.

C. Adaptive Choice of Regularization Parameters

The regularization parameter λ of the energy functionals in (15) and (16) controls the tradeoff between the goodness of fit of f and the smoothing. When λ is too large, insufficient smoothing is undertaken to remove the speckle, whereas when λ is too small, more noise is removed but with the loss of too many image features. The basic idea of the adaptive functional models in this study is to adaptively find appropriate values of λ based on both the local heterogeneity information of each pixel (spatial adaptivity) and the noise level (noise adaptivity).

There is generally a tradeoff between speckle reduction and detail preservation. When removing speckle from an image, the details are often severely reduced. A number of studies [34], [35] have shown that an approach to partially alleviate this problem is to use spatial adaptivity. The general idea of this approach is to exert less smoothing for edges and features, and more smoothing for homogeneous areas. In this paper, we employ the local homogeneity index (LHI) in the Lee filter [3] to realize the spatial adaptivity of λ.

An important property of speckle is that the ratio of the intensity's standard deviation to the mean [or coefficient of variation (σ_v)] is a constant for a given number of looks L

$$\sigma_v = \sqrt{\frac{1}{L}}. \tag{17}$$

The LHI is derived based on this property

$$\text{LHI} = \frac{\text{var}(f_{\text{sub}}) - (\bar{f}_{\text{sub}} \cdot \sigma_v)^2}{(1 + \sigma_v^2)\,\text{var}(f_{\text{sub}})} \tag{18}$$

where $\text{var}(f_{\text{sub}})$ and $\bar{f}_{\text{sub}}$, respectively, denote the variance and mean of the observed image computed over a 3 × 3 window centered on the target pixel. LHI may become negative due to insufficient samples. If so, it should be set to zero to ensure that it is between 0 and 1. For a pixel x in a homogeneous area, $\text{LHI}(x) \approx 0$; for a pixel located in a heterogeneous area with highly contrasting edges or features, $\text{LHI}(x) \approx 1$. Finally, the spatially adaptive regularization parameter can be obtained as

$$\lambda(x) = \text{LHI}(x) \times \lambda_0. \tag{19}$$

By considering the local heterogeneity information, the proposed spatially adaptive λ can enhance the image details while smoothing the homogeneous regions.

$$u_{n+1}(x)=u_n(x)-\frac{F_1\left(u_n(x)\right)}{F_1'\left(u_n(x)\right)}=u_n(x)-\frac{\int_\Omega \frac{\frac{1}{2}[u_n(x)-u_0(y)]}{u_n(x)+u_0(y)}\cdot\exp\left\{-\left[\frac{\log\frac{u_0(x)+u_0(y)}{\sqrt{u_0(x)u_0(y)}}}{h}\right]^2\right\}dy+\lambda(x)\left(-\frac{f(x)}{u_n(x)}+1\right)}{\int_\Omega \frac{u_0(y)}{[u_n(x)+u_0(y)]^2}\cdot\exp\left\{-\left[\frac{\log\frac{u_0(x)+u_0(y)}{\sqrt{u_0(x)u_0(y)}}}{h}\right]^2\right\}dy+\frac{\lambda(x)f(x)}{[u_n(x)]^2}} \tag{24}$$

One issue that should be addressed is the choice of the initial value of λ_0. Generally speaking, for serious noise, a small value of λ should be chosen to sufficiently smooth the image; for low noise, a large value of λ is appropriate for fitting the observed image, which means that λ_0 can be set based on the level of the noise. Therefore, in this study, a simple linear relationship is proposed to set λ_0 automatically, based on the noise level, as

$$\lambda_0 = \frac{L}{k} \tag{20}$$

where k is a scalar parameter.

IV. IMPLEMENTATION OF THE ANLF MODELS

1) Implementation of the NHANLF Model

The variation with respect to u of the nonhomomorphic nonlocal functional J_1 in (15) is

$$F_1 = \lambda(x)\left(-\frac{f(x)}{u^2(x)}+\frac{1}{u(x)}\right)+\int_\Omega \frac{\frac{1}{2}\left[u(x)-u(y)\right]}{\left[u(x)+u(y)\right]u(x)} \cdot \exp\left\{-\left[\frac{\log\frac{v_1(x)+v_1(y)}{\sqrt{v_1(x)v_1(y)}}}{h}\right]^2\right\}dy. \tag{21}$$

Discarding the same terms $u(x)$ in the denominator, F_1 can then be reduced to

$$F_1 = \lambda(x)\left(-\frac{f(x)}{u(x)}+1\right)+\int_\Omega \frac{\frac{1}{2}\left[u(x)-u(y)\right]}{u(x)+u(y)} \cdot \exp\left\{-\left[\frac{\log\frac{v_1(x)+v_1(y)}{\sqrt{v_1(x)v_1(y)}}}{h}\right]^2\right\}dy. \tag{22}$$

The estimated value of each pixel x can then be obtained by solving the Euler–Lagrange equation: $F_1(u(x)) = 0$. To quickly solve this nonlinear equation, we choose the Newton iteration method [36] for its traits of high computational efficiency and ease of operation.

Given a single-variable nonlinear equation, $F(a) = 0$, the iteration scheme of the Newton method for solving the equation is as follows:

$$a_{n+1} = a_n - \frac{F(a_n)}{F'(a_n)} \tag{23}$$

where $F'(\cdot)$ denotes the derivative of $F(\cdot)$ with respect to the variable a and a_n is the approximate solution of the equation calculated at the nth iteration. Hence, the Newton iteration scheme for solving $F_1(u(x)) = 0$ is given by (24), shown at the top of the page, where $u_0(y)$ is the pixel value of y in the speckled image and $u_n(x)$ is the value of x in the denoised image of the nth iteration. It must be noted that two issues should be of concern when applying the Newton method to solve the equation. How many solvers does the equation have in the definition domain? Which solver of the Euler–Lagrange equation minimizes the energy functional? In fact, the Euler equation of the nonhomomorphic ANLF (NHANLF) model has only one positive solver, and this solver minimizes J_1. We refer the readers to the Appendix for the proof of the aforementioned conclusion and the uniqueness of the minimizer of the NHANLF model.

Finally, as in the similar procedure in [37], we set $u^0(x) = f(x)$ and perform a fixed-point iteration to obtain the final restored images

$$u^{i+1}(x) = F_1^*\left(u^i(x)\right) \tag{25}$$

where $F_1^*(u^i(x))$ denotes the solver of the Euler equation $F_1(u^i(x)) = 0$ calculated by (24), or in other words, in each fixed-point iteration, the Newton method is employed to obtain a cleaner image, which is set as the image to be denoised in the next fixed-point iteration.

As pointed out in [30], in the nonlocal functional models, a better way of constructing the weight function is to use a preprocessed image instead of the blurry and noisy data f, which means that, in each fixed-point iteration, it is better to calculate the weights using the restored image of the last fixed-point iteration as the reference.

To sum up, the detailed implementation scheme of the NHANLF model is as follows: for the pixel x, its restored value in the $n+1$th Newton iteration of the ith fixed-point iteration is obtained by (26), shown at the top of the next page, where the superscript of u denotes the fixed-point iteration number and the subscript of u denotes the Newton iteration number, which are defined in the same way in the rest of this paper. The Newton iteration process in the ith fixed-point iteration is stopped if the following condition is satisfied:

$$\frac{\left|u_{n+1}^i(x) - u_n^i(x)\right|}{u_n^i(x)} < 0.001. \tag{27}$$

$$u_{n+1}^{i}(x) = u_{n}^{i}(x) - \frac{F_1\left(u_n^i(x)\right)}{F_1'\left(u_n^i(x)\right)} = u_n^i(x) - \frac{\int_\Omega \frac{\frac{1}{2}\left[u_n^i(x)-u_0^i(y)\right]}{u_n^i(x)+u_0^i(y)} \cdot \exp\left\{-\left[\frac{\log\frac{u_0^i(x)+u_0^i(y)}{\sqrt{u_0^i(x)u_0^i(y)}}}{h}\right]^2\right\} dy + \lambda(x)\left(-\frac{f(x)}{u_n^i(x)}+1\right)}{\int_\Omega \frac{u_0^i(y)}{\left[u_n^i(x)+u_0^i(y)\right]^2} \cdot \exp\left\{-\left[\frac{\log\frac{u_0^i(x)+u_0^i(y)}{\sqrt{u_0^i(x)u_0^i(y)}}}{h}\right]^2\right\} dy + \frac{\lambda(x)f(x)}{\left[u_n^i(x)\right]^2}} \tag{26}$$

$$\begin{aligned} E_{n+1}^{i}(x) &= E_n^i(x) - \frac{F_2\left(E_n^i(x)\right)}{F_2'\left(E_n^i(x)\right)} \\ &= E_n^i(x) - \frac{\int_\Omega 2\left[E_n^i(x) - E_0^i(y)\right] \exp\left\{-\left[\frac{E_0^i(x)-E_0^i(y)}{h}\right]^2\right\} dy + \lambda(x)\left\{-f(x)\exp\left[-E_n^i(x)\right]+1\right\}}{\int_\Omega 2\exp\left\{-\left[\log\frac{E_0^i(x)-E_0^i(y)}{h}\right]^2\right\} dy + \lambda(x)f(x)\exp\left[-E_n^i(x)\right]} \end{aligned} \tag{30}$$

---

2) Implementation of the HANLF Model

The variation with respect to E of the homomorphic nonlocal functional J_2 in (16) is

$$F_2 = \lambda(x)\left[-f(x)e^{-E(x)}+1\right] + \int\limits_\Omega 2\left[E(x)-E(y)\right]\exp\left\{-\left[\frac{v_2(x)-v_2(y)}{h}\right]^2\right\} dy. \tag{28}$$

It can also be proved that this equation has only one solver which minimizes the energy functional J_2 (see the Appendix). We then set $E^0 = \log f$ and perform a fixed-point iteration

$$E^{i+1}(x) = F_2^*\left(E^i(x)\right) \tag{29}$$

where $F_2^*(E^i(x))$ denotes the solver of the Euler equation $F_2(E^i(x)) = 0$ calculated by the Newton method. To sum up, for the log-transformed pixel x, its restored value in the $n+1$th Newton iteration of the ith fixed-point iteration is obtained by (30), shown at the top of the page.

V. EXPERIMENTAL PART

In this section, to illustrate the performances of the proposed ANLF models, the results obtained with five simulated SAR images and two real SAR image are reported. In this paper, the size of the proposed methods' searching window was fixed as 21 × 21 for all of the tested images. First, several variational models were implemented to compare with the proposed ANLF models: the AA model [6], the spatially adaptive AA (SAA) model [34], the SO model [23], and a new convex variational model proposed by Zhao *et al.* [28]. We then compared the proposed models with two state-of-the-art techniques based on the nonlocal approach: the probabilistic patch-based (PPB) filter [10] and the SAR block-matching 3-D (SAR-BM3D) algorithm [14].

A. Comparison With Other Variational Models on Five Simulated and Two Real SAR Images

1) Experiments on Simulated SAR Images: The use of simulated SAR data allows an objective performance assessment of the speckle suppression efficiency. To achieve this goal, the common approach in the literature is to use a virtually noiseless optical image as a clean reference and to inject a speckle field with proper statistics on it. However, this approach clearly has some shortcomings, as the statistics of a SAR image are very different from other types of images, including the dynamics, gray-level distribution, spatial correlation, operational wavelengths, and so on. Recently, Di Martino *et al.* [38] have proposed a framework for the objective assessment of SAR despeckling techniques, based on the simulation of SAR images relevant to canonical scenes. In this framework, each image is generated using a complete SAR simulator that includes proper physical models for the sensed surface, the scattering, and the radar operational mode. Through simulating multiple SAR images as different instances relevant to the same scene, SAR images with an arbitrary number of looks can be obtained. This simulation method is based on a SAR raw signal simulator (SARAS) [39], and it is based on sound geometrical and electromagnetic models for the evaluation of the reflectivity function of the scene and on a model for the transfer function of the system, which are used for the evaluation of the raw signal. In this paper, we used five SAR images simulated by this framework and the indicators proposed in [38] to inspect the despeckling performances of the proposed techniques. All of the simulated images and the scripts used to calculate the indicators are available for download at http://www.grip.unina.it/. The following part is a basic description of the simulated images and the used indicators. For more detailed information about the images and indicators, readers can refer to [38].

1) The first image is the "Homogeneous" image. This image is used to simulate a single flat region with constant electromagnetic parameters. This is the simplest, yet most important, canonical scene, as it allows the user to assess the speckle reduction ability of a filtering technique. To this end, we employ the widely used equivalent number of looks (ENL) to characterize the amount of smoothing in homogeneous areas. Furthermore, we also use two bias indicators: the mean value and the variance of the ratio image between the noisy and filtered images. For an ideal filter, its ratio image should be pure speckle. Therefore, in this study, a mean of ratio (MoR) significantly different from one indicates some radiometric distortion. The variance of ratio (VoR) provides an insight into the under/oversmoothing phenomena. A VoR < 1 indicates undersmoothing, whereas a VoR > 1 indicates oversmoothing.
2) The second image is the "Squares" image. This image contains several regions of flat terrain, separated by straight contours, and is characterized by different electromagnetic parameters. By using this image, we can inspect the capabilities of the despeckling methods in preserving the edges and boundaries between different land objects. To describe the degradation of edges, the edge smearing (ES) and Pratt's FOM indexes [40] are used. The ES is computed as the weighted square error between the edge profiles (EPs) of the filtered image $\hat{u}$ and reference image u

$$\text{ES} = \int g(t-t_0)\left(\text{EP}_{\hat{u}}(t) - \text{EP}_u(t)\right)^2 dt \tag{31}$$

where $g(t-t_0)$ is a Gaussian kernel that allows us to assign a larger weight to errors that occur near the edge location t_0, which can prevent the speckle in the homogeneous areas from affecting the edge degradation measure. Differing from ES, the FOM index is calculated only considering the edge pixels. The FOM index is defined as

$$\text{FOM} = \frac{1}{\max(n_d, n_r)} \sum_{i=1}^{n_d} \frac{1}{1+\gamma d_i^2} \tag{32}$$

where n_d and n_r are, respectively, the number of edge pixels detected in the despeckled and reference image, d_i is the Euclidean distance between the ith detected edge pixel of the despeckled image and the nearest reference edge pixel, and the parameter γ, which is set as 1/9, as in [38], modulates the cost of edge displacement. A larger FOM value indicates superior edge rendition.
3) The third image is the "Corner" image. This image simulates a corner reflector placed on a homogeneous background. In high-resolution SAR images, trihedral structures often act as corner reflectors, which show high-intensity returns on the images. A good despeckling method should not significantly modify the corner reflector response. In this case, to assess the radiometric preservation of the filtering process, we use the C_{NN} and C_{BG} indicators, which are defined as

$$C_{NN} = 10\log_{10}\frac{u_{CF}}{u_{NN}} \tag{33}$$

$$C_{BG} = 10\log_{10}\frac{u_{CF}}{u_{BG}} \tag{34}$$

where u_{CF}, u_{NN}, and u_{BG} are the intensity observed in the corner reflector site, the average intensity in the surrounding region formed by the eight connected nearest neighbors, and the average intensity of the background, respectively. For a good filter, these two indicators should be close to the corresponding numbers computed on the reference image.
4) In the fourth test case, we simulate a "Building" image, with an isolated building placed on a homogeneous background. It is important to preserve the position and radiometric characteristics of building radar returns when choosing a filtering technique. For the assessment of the radiometric preservation, the C_{DR} indicator is employed

$$C_{DR} = 10\log_{10}\frac{u_{DR}}{u_{BG}} \tag{35}$$

where u_{DR} denotes the average intensity computed on the building radar returns. For a filter that can effectively preserve the high signal returns of a building, the C_{DR} indicator should be close to the corresponding number computed on the reference image. To quantify the preservation of the building profile (BP), we employ the building smearing (BS) index, which is defined as

$$\text{BS} = \int \prod\left(\frac{t-t_0}{T}\right) \left|\log_{10}\left(\text{BP}_{\hat{u}}(t)+\varepsilon\right) - \log_{10}\left(\text{BP}_u(t)+\varepsilon\right)\right| dt \tag{36}$$

where ε is a small positive value. This index is computed by averaging along the azimuth direction and integrates the absolute difference with respect to the clean profile in a small range centered on the double reflection line.
5) The last simulated image is the "Digital Elevation Model (DEM)" image, with a single region with constant electromagnetic parameters but nonflat orography. In this case, we use two indicators to compare the filtering methods: the coefficient of variation (C_x) and the DG indicator, which is defined as

$$\text{DG} = 10\log_{10}\left(\frac{\text{MSE}(u,f)}{\text{MSE}(u,\hat{u})}\right) \tag{37}$$

where u, $\hat{u}$, and f are, respectively, the clean image, the filtered image, and the speckled image. MSE denotes the traditional mean-square error. A larger value of the DG indicator indicates better speckle rejection. For a good filter which can effectively preserve texture, the C_x estimated for the filtered image by means of the spatial averages should be close to the value expected for the original image.

For each of the previously described images, we tested the filtering methods on eight different instances (eight different single-look images) relevant to the same scene and obtained

TABLE I

QUANTITATIVE ASSESSMENT RESULTS FOR THE SIMULATED IMAGES FILTERED BY THE DIFFERENT VARIATIONAL METHODS

		AA model	SAA model	SO model	Zhao's model	HANLF model	NHANLF model	Reference
Homogeneous	ENL	48.4	55.1	86.9	89.0	**112.4**	111.5	/
	MoR	0.91	0.95	1.81	0.86	0.91	**0.98**	/
	VoR	0.21	0.30	10.52	4.01	0.82	**0.84**	/
Squares	ES_up	0.25	0.24	0.58	0.06	0.72	**0.05**	/
	ES_down	0.73	0.78	1.66	**0.02**	0.93	0.12	/
	FOM	0.70	0.73	0.70	**0.81**	0.69	0. 80	/
Corner	C_{NN}	7.96	7.52	1.15	**7.76**	7.61	8.21	7.75
	C_{BG}	33.78	36.39	9.82	35.88	36.76	**36.41**	36.56
Building	C_{DR}	**65.89**	66.56	62.85	64.60	67.02	66.22	65.90
	BS	6.97	5.50	5.97	7.35	3.02	**2.89**	/
DEM	C_x	3.13	2.85	1.91	1.84	2.99	**2.50**	2.40
	DG	2.01	2.98	**5.80**	5.49	5.53	5.44	/

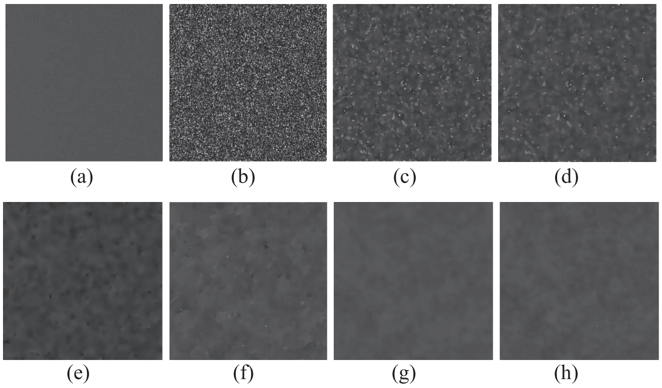

Fig. 1. Despeckling results on the "Homogeneous" image. (a) Reference image. (b) Single-look speckled image. The images despeckled by (c) the AA model, (d) the SAA model, (e) the SO model, (f) Zhao's model, (g) the HANLF model, and (h) the NHANLF model.

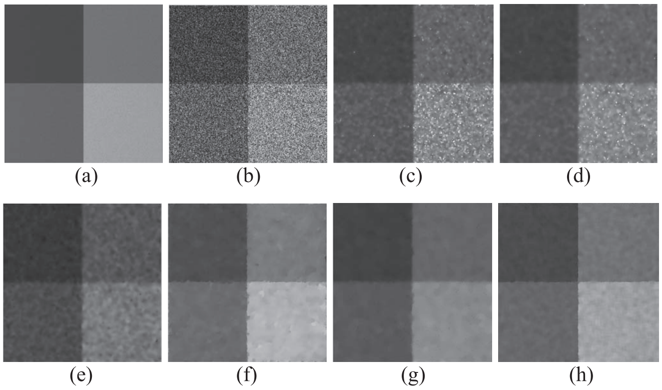

Fig. 2. Despeckling results on the "Squares" image. (a) Reference image. (b) Single-look speckled image. The images despeckled by (c) the AA model, (d) the SAA model, (e) the SO model, (f) Zhao's model, (g) the HANLF model, and (h) the NHANLF model.

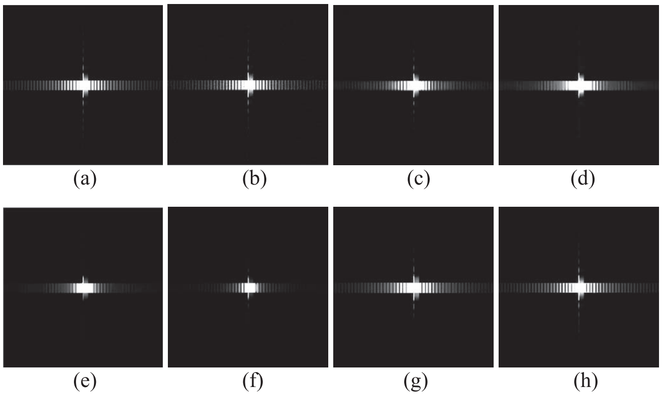

Fig. 3. Despeckling results on the "Building" image. (a) Reference image. (b) Single-look speckled image. The images despeckled by (c) the AA model, (d) the SAA model, (e) the SO model, (f) Zhao's model, (g) the HANLF model, and (h) the NHANLF model.

the quantitative results by averaging the assessment results of these eight different instances, and we used a 512-look image as a reference image. To fairly compare the performances of the despeckling techniques, the parameters of each filtering method were fixed for all of the test cases. Table I lists the quantitative assessment results of the methods on the simulated images. To improve the readability, for each indicator in the table, we use a boldface number to indicate the best filtering result and underlining to indicate the second-best filtering result. Figs. 1, 2, 3, 5, and 8 show the despeckling results of the variational methods on one realization of each test image, respectively.

First, it can be seen that, generally speaking, the proposed NHANLF model can achieve better despeckling performances than the homomorphic ANLF (HANLF) model from both the quantitative indexes and the visual result. The reason for this may be that, as we stressed in Section III, the homomorphic nonlocal functional is derived with the assumption that the log-transformed speckle is Gaussian distributed. The log-transformed speckle follows a Fisher–Tippett distribution, which can be effectively fitted by a Gaussian distribution only when the noise is not serious. This means that the Gaussian hypothesis about the log-transformed speckle could be more inclined to result in unsatisfactory results when the number of looks is small.

For the despeckled "Homogeneous" image, it is quite easy to visually assess the speckle reduction ability of the different techniques. All of the conventional variational methods show some artifacts, especially Zhao's model and the SO model. Compared with the other four models, the AA model and the SAA model do not effectively reduce the speckle. The ENL values listed in Table I confirm the good speckle reduction ability of the proposed methods. Furthermore, the MoR values

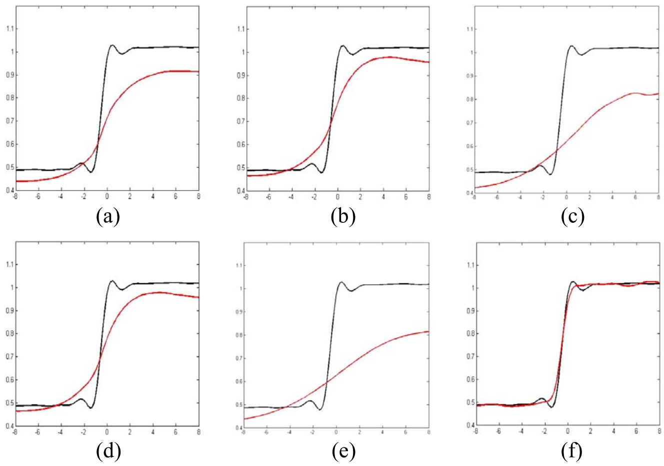

Fig. 4. EPs (upper edges) obtained for the six methods (red) compared with the reference one (black). (a) AA model. (b) SAA model. (c) SO model. (d) Zhao's model. (e) HANLF model. (f) NHANLF model.

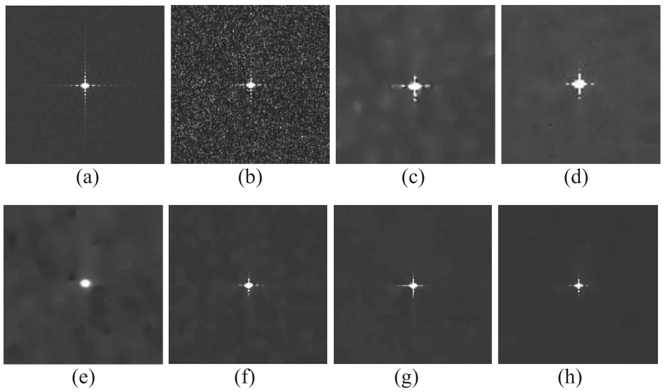

Fig. 5. Despeckling results on the "Corner" image. (a) Reference image. (b) Single-look speckled image. The images despeckled by (c) the AA model, (d) the SAA model, (e) the SO model, (f) Zhao's model, (g) the HANLF model, and (h) the NHANLF model.

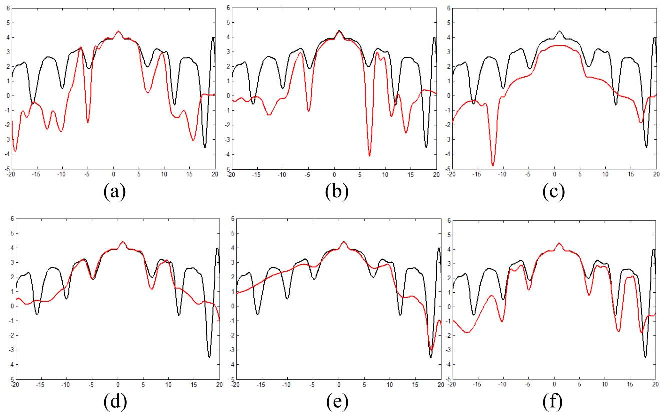

Fig. 6. Range profiles of the corner reflector obtained by the six methods (red) compared with the reference one (black). (a) AA model. (b) SAA model. (c) SO model. (d) Zhao's model. (e) HANLF model. (f) NHANLF model.

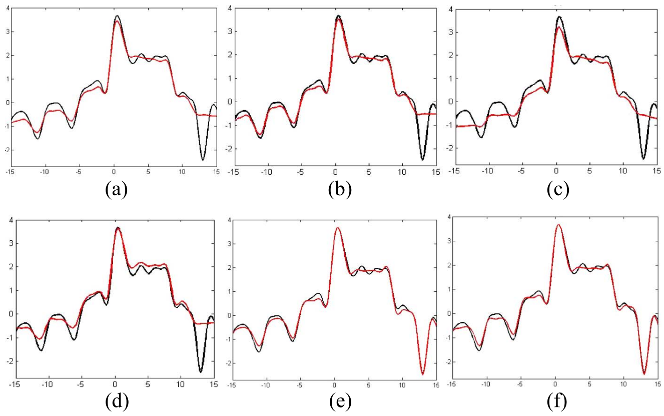

Fig. 7. Range profiles of the building obtained by the six methods (red) compared with the reference one (black). (a) AA model. (b) SAA model. (c) SO model. (d) Zhao's model. (e) HANLF model. (f) NHANLF model.

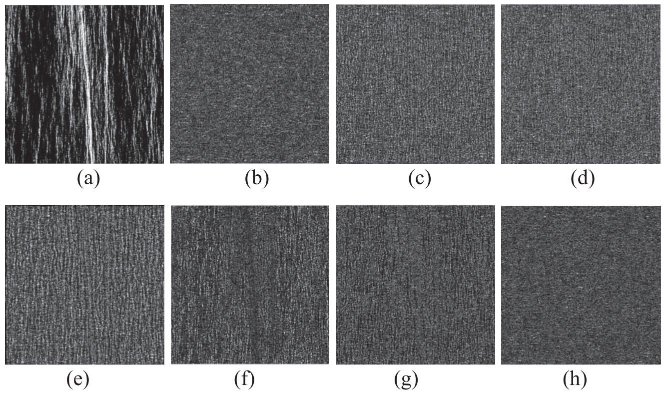

Fig. 8. (a) Reference "DEM" image. The ratio images for (b) the reference, (c) the AA model, (d) the SAA model, (e) the SO model, (f) Zhao's model, (g) the HANLF model, and (h) the NHANLF model.

indicate that the AA model, the SAA model, and the proposed models perform better in radiometric preservation.

For the "Squares" image, Table I reports the ES figures for the two vertical edges, characterized by lower (up) and higher (down) contrasts. The AA model does not effectively reduce the speckle, and it results in a slight blocky appearance, which is a problem that many variational methods often encounter. The SAA model generally outperforms the AA model due to its spatially adaptive strategy. Compared with the SAA model, the SO model clearly performs better in reducing speckle, but it badly smears the boundaries, which can be seen in its poor results for the ES and FOM indicators. Zhao's convex variational model and the proposed HANLF model reduce the speckle to a greater degree, but both methods have problems: the image filtered by Zhao's model shows an evident blocky problem and staircase effect, which may be undesirable in some applications, and the HANLF model results in an oversmoothing problem and smears the edges to some extent. Compared with the aforementioned variational methods, the proposed NHANLF method not only effectively suppresses the speckle but also enhances and retains the edges. To visualize the capability of the variational methods in preserving edges, we plot the EPs for each filtered image in Fig. 4. The conclusion that we can draw from this figure is generally in line with the observation for Fig. 2 and Table I: Zhao's model and the NHANLF model perform best in preserving edges, and the SO model and HANLF model perform poorly in preserving edges.

For the "Corner" image, the measures of interest are aimed at evaluating the radiometric preservation by using C_{NN} and C_{BG}. One can see from Fig. 5 that some filtering phenomena,

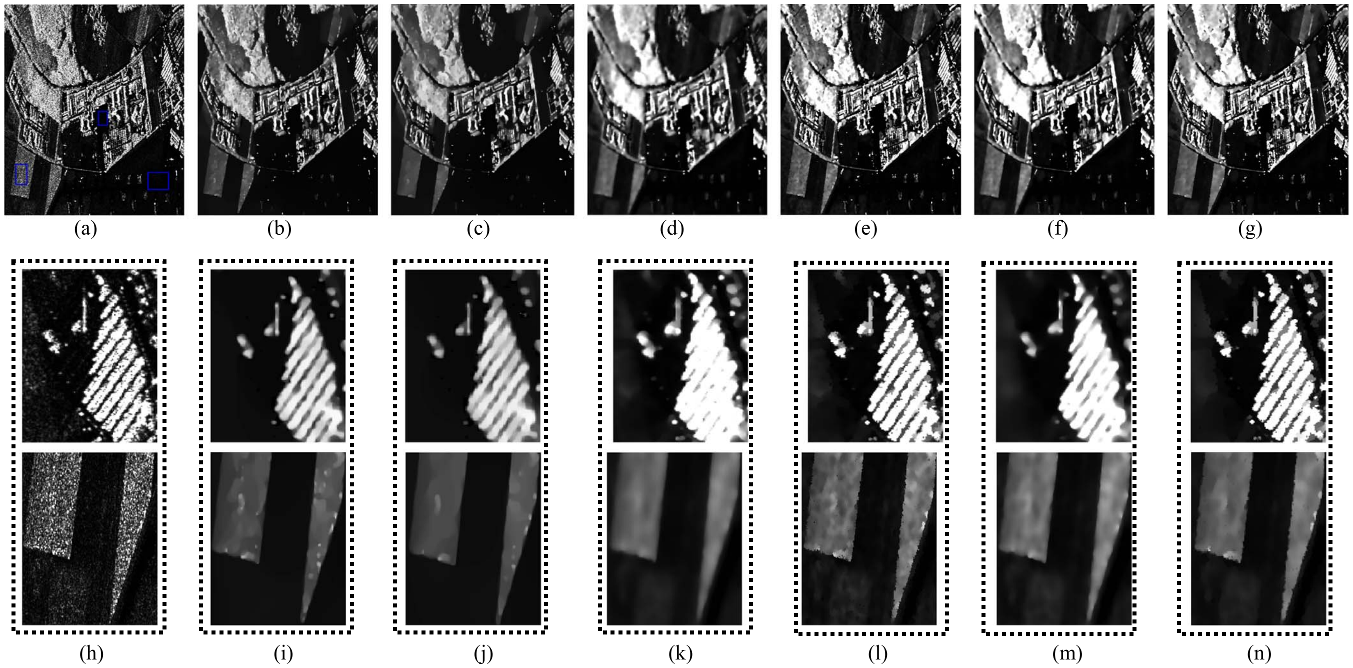

Fig. 9. Comparison of the despeckling performances with the Oberpfaffenhofen image. (a) Speckled image. The image restored by (b) the AA model, (c) the SAA model, (d) the SO model, (e) Zhao's convex variational model, (f) the HANLF model, and (g) the NHANLF model. (h)–(n) Subimages cropped from (a)–(g), respectively.

like those observed with the "Squares" image, are still evident: the blocky problem remains in the AA model filtered image, and the SO model badly smears the image features. This conclusion can also be made from Fig. 6, which shows the range profile of the corner reflector of each filtered image compared with the reference one. Except for the SO model, all of the other models can generally retain some of the high returns of the corner responses to a greater or lesser degree. Visually, Zhao's method and the two proposed methods show comparable filtering results. From the numerical indicators, it can be seen that Zhao's model and the NHANLF model perform the best in radiometric preservation among these six models.

For the "Building" image, it is evident that the SO model and Zhao's model badly smear some building profiles with relatively low values, and the other two conventional variational models show an oversmoothing problem. The two proposed models obtain better results in preserving the building profiles, although the AA model is the best at radiometric preservation, as revealed by the C_{DR} indicator. As in the "Squares" and "Corner" images, we also plot the range profiles of the buildings of each filtered image compared with the reference one in Fig. 7. Here, it can be seen that the proposed models show desirable and comparable results, while the other four conventional models change the profiles of the buildings.

For the last case, the "DEM" image, distinguishing the speckle from the high-frequency signal components is a challenging task. To better reveal the despeckling performance of the different methods on the "DEM" image, we show the ratio images between the noisy image and the despeckled images in Fig. 8. For an ideal filter, its ratio image should be pure speckle. In Fig. 8, it can be seen that the ratio image for the NHANLF model has the appearance of random noise, which indicates the NHANLF model's good capability in preserving DEM details. This conclusion can also be made from the C_x values listed in Table I. Vertical DEM structures are recognizable in the other five ratio images, especially in the ratio images for the SO model and Zhao's model, which proves that some DEM details are filtered out by these methods. The DG indicator shows that the AA model and the SAA model still do not effectively suppress the speckle.

2) Experiments on Real SAR Images: Two real SAR images were also used for illustration in this study. One was a single-look image acquired by the DLR Experimental Synthetic Aperture Radar (ESAR) system over the area of Oberpfaffenhofen airport near Munich, Germany. The other was a subimage of a four-look Airborne Synthetic Aperture Radar (AIRSAR) data set from Flevoland in The Netherlands. Figs. 9 and 10 show the despeckling results on these two images. The areas chosen for computing the ENL are indicated by blue rectangles in the speckled images. As expected, the image filtered by the AA model shows a blocky effect, and the edges are blurred. The SAA model alleviates the blocky problem and achieves a better performance in reducing speckle than the AA model (Table II). The SO model shows positive despeckling results in homogeneous areas; however, the despeckled image is badly oversmoothed. Zhao's convex variational model shows better results in retaining the edges, but the degree of speckle in the restored image is relatively high; in addition, the blocky appearance in the despeckled image leads to the problem of blurring of some strong point targets [Fig. 10(e)].

Compared with the aforementioned variational methods, the proposed methods obtain better despeckling results, and they also effectively preserve and enhance the edges. One can also observe in Figs. 9 and 10 that, for the four-look Flevoland image, the homomorphic model and the nonhomomorphic model

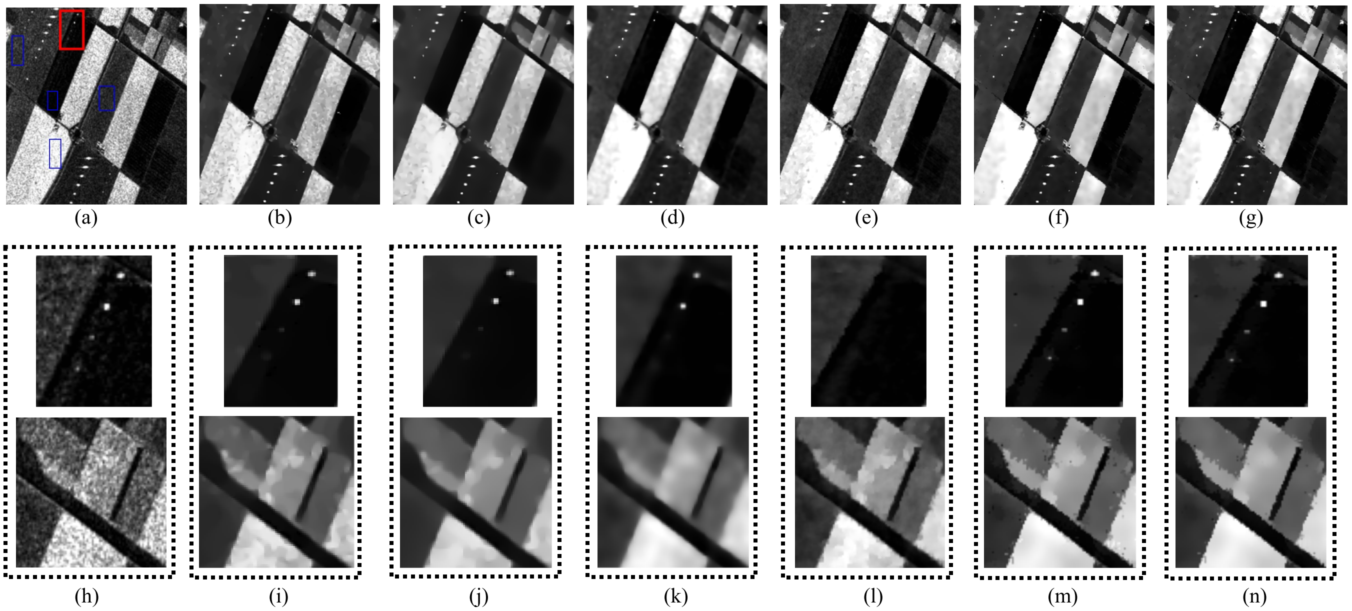

Fig. 10. Comparison of the despeckling performances with the Flevoland image. (a) Speckled image. The image restored by (b) the AA model, (c) the SAA model, (d) the SO model, (e) Zhao's model, (f) the HANLF model, and (g) the NHANLF model. (h)–(n) Subimages cropped from (a)–(g), respectively.

TABLE II
ENL FOR THE REAL SAR IMAGES FILTERED BY THE DIFFERENT VARIATIONAL METHODS

	AA model	**SAA model**	**SO model**	**Zhao's model**	**HANLF**	**NHANLF**
Oberpfaffenhofen image	32.0	36.7	**46.1**	34.1	*44.9*	44.0
Flevoland image	38.4	42.7	46.0	41.7	*47.2*	**47.5**

achieve quite comparable results; however, for the single-look image, the superiority of the nonhomomorphic model is much more obvious. This once again demonstrates the point that we made before in that the Gaussian hypothesis about the log-transformed speckle could be more inclined to bring in unsatisfactory results for the HANLF model when the noise level is high.

Preservation of strong returns from point targets is essential for target and man-made structure detection. In certain SAR filtering algorithms [7], isolated point targets are detected and are kept unfiltered. Although, in the proposed methods, no special strategies are deployed to detect and retain these targets, we undertook an experiment to show that the proposed methods are able to preserve them. A line was taken across four high-return point targets [marked by the red rectangle in Fig. 10(a)], and the intensity values of this line after despeckling by the different methods are plotted in Fig. 11. Here, it can be observed that the original data are almost overlapped at strong point target locations by the proposed NHANLF model, which indicates the proposed method's ability to retain strong point targets. The other methods smear the point target signatures to a greater or lesser degree.

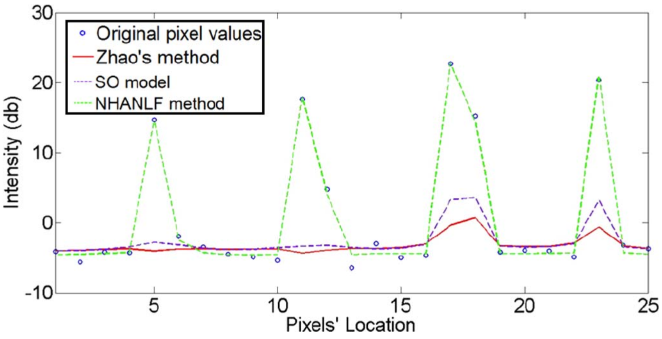

Fig. 11. Profiles of a line across some point targets in the Flevoland image after restoration by the different methods.

B. Comparison With Other State-of-the-Art Methods

To further validate the despeckling performance of the NHANLF model, we compared the proposed method with two state-of-the-art techniques: the PPB filter [10] and SAR-BM3D [14]. The PPB filter is a kind of "iterative nonlocal means" method with iteratively refined weights, which are calculated by considering both the information in the original speckled image and the information in the previous estimates. SAR-BM3D is the SAR-oriented nonhomomorphic version of the original BM3D algorithm for AWGN images. Its main modifications consist of the similarity measure used in the block matching and the local linear MMSE estimator in the frequency domain used in both steps of the procedure.

For the simulated SAR images, we used the same parameters as [38] for the PPB and SAR-BM3D filters, and we only report their quantitative assessment results due to the space limitations. Readers can refer to [38] to gain an insight into the filtering performances of these five images. One can observe from Table III that, although SAR-BM3D generally shows the best performances in filtering the simulated SAR images, the proposed method can also obtain a competitive filtering

TABLE III
PERFORMANCE COMPARISON BETWEEN THE PROPOSED METHOD AND THE OTHER STATE-OF-THE-ART METHODS

			PPB	**SAR-BM3D**	**NHANLF model**
Simulated image	***Homogeneous***	ENL	**127.7**	102.4	111.5
		MoR	0.96	**0.98**	0.91
		VoR	0.82	0.81	**0.84**
	Squares	ES_up	0.07	**0.04**	0.05
		ES_down	0.21	**0.11**	0.12
		FOM	0.84	**0.85**	0.80
	Corner	C_NN Reference (7.75)	3.75	**7.39**	8.21
		C_BG Reference (36.56)	32.69	35.45	**36.41**
	Building	C_DR Reference (65.90)	64.90	**65.91**	66.22
		BS	3.13	**1.46**	2.89
	DEM	C_x Reference(2.40)	2.71	**2.43**	2.50
		DG	3.68	5.32	**5.44**
Real image	***Oberpfaffenhofen***	ENL	*43.5*	42.1	**44.0**
	Flevoland	ENL	**47.7**	46.8	*47.5*

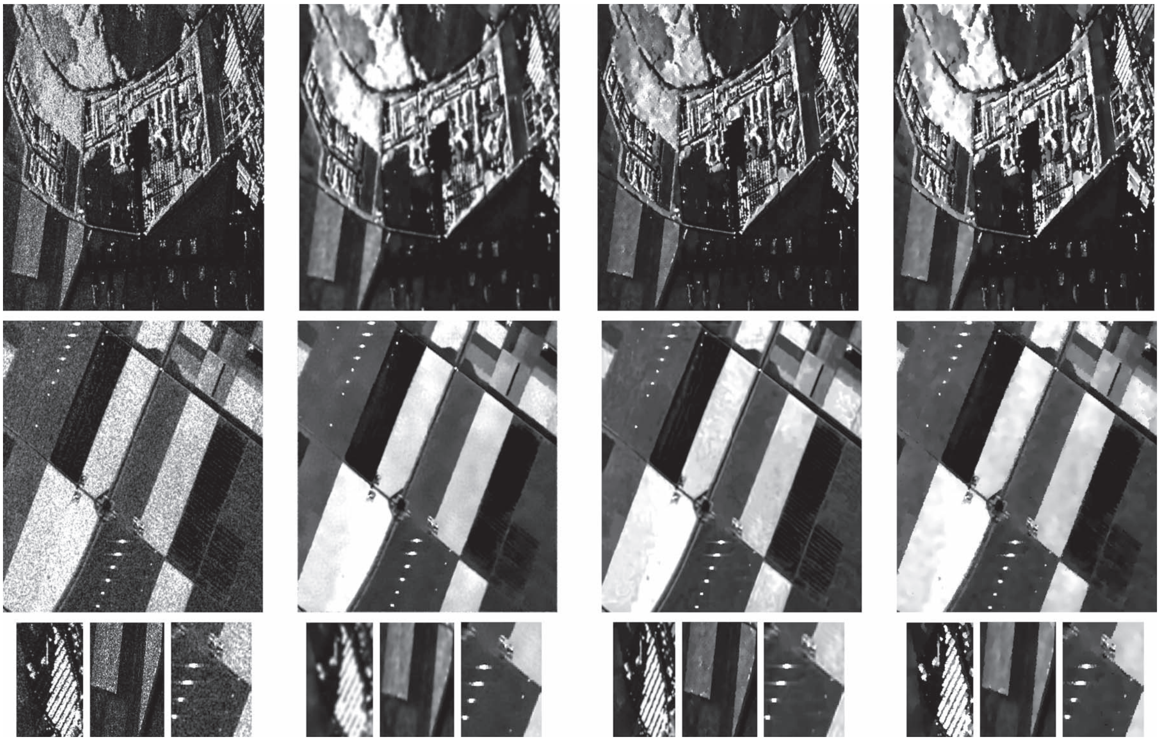

(a) (b) (c) (d)

Fig. 12. (a) From top to bottom: the Oberpfaffenhofen image, the Flevoland image, and the subimages. The corresponding restored images by (b) the PPB filter, (c) SAR-BM3D, and (d) the NHANLF model.

result. For the "Homogeneous" and "Squares" images, the PPB filter suppresses the speckle to the greatest degree, while SAR-BM3D performs the best in preserving edges. The proposed NHANLF method seems to be a compromise between the PPB filter and SAR-BM3D. For the "Corner" image and the "Building" image, the C_{NN}, C_{BG}, and C_{DR} indicators suggest that SAR-BM3D and the proposed method are superior to the PPB filter in radiometric preservation of high returns. The BS index indicates the superiority of SAR-BM3D in retaining object profiles. For the "DEM" image, SAR-BM3D once again performs the best in preserving image structures and details, as revealed by the C_x indicator; the DG indicator, however, illustrates that the NHANLF method performs the best in removing speckle from this complicated image.

Fig. 12 shows the filtering results of the three methods on the two real SAR images. One can see that, generally speaking, the three methods all show quite positive and comparable filtering performances: speckle is suppressed to a large degree, and most of the structures and details of the images are preserved. From Fig. 12(b), we can see that, compared with SAR-BM3D and NHANLF, the PPB filter seems to result in slight oversmoothing, which degrades its performance in preserving edges to some extent. SAR-BM3D not only reduces the speckle, but it performs better in retaining image details than the PPB filter.

TABLE IV
COMPUTATION TIMES OF THE DIFFERENT METHODS WITH THE OBERPFAFFENHOFEN IMAGE (SECONDS)

PPB	SAR-BM3D	HANLF	NHANLF
1200.7	1344.2	594.3	928.0

Visually, the NHANLF method looks like a compromise between the aforementioned two filters, especially for the single-look Oberpfaffenhofen image.

In addition to the performance in suppressing speckle and retaining details, the computation time and storage efficiency are also important indexes to assess the applicability of despeckling algorithms. For many high-resolution SAR systems, such as the TerraSAR-X and Cosmo-SkyMed SAR systems, their image dimensions can be $10\,000 \times 10\,000$ pixels. Future spaceborne SAR systems are expected to have even higher dimensions. Therefore, a rapid and memory-saving despeckling algorithm is necessary. In Table IV, to inspect the computational efficiency of the proposed models, we report the computation times of the proposed models, the PPB filter, and SAR-BM3D with the Oberpfaffenhofen image (1540×2816 pixels). The source codes of the PPB filter and SAR-BM3D were downloaded online and were implemented in C++ with a MATLAB interface, while the proposed methods were implemented and run in MATLAB.

First, we can see from Table IV that HANLF is much faster than NHANLF. This is because the log-transformation step compresses the data range, which accelerates the speed of convergence for the HANLF model. Although it may be unfair to directly compare the computational efficiency of our methods with those of the two other methods as they are implemented in different platforms, we can qualitatively analyze their computational complexity. SAR-BM3D contains two estimation steps. In each step, similar patches in the large nonlocal searching window centered on the reference patch are stacked to form a group, all of the pixels in each group are then filtered by a wavelet-based filter and are returned to their original location, and finally, each pixel in the image is filtered by the weighted averaging of the estimates which are obtained from the different groups. This nonlocal 3-D collaborative filtering strategy results in a heavy memory and computational load. The computation time of the PPB filter and the proposed methods is associated with the amount of speckle in the images: the more intense the noise, the slower the convergence. We found that, in most cases, for a single-look speckled image, the number of iterations of the PPB filter was about 20, while the number of fixed-point iterations of the NHANLF model was about 10. Meanwhile, Newton iteration has the trait of fast convergence, and we found that the average number of Newton iterations in the first fixed-point iteration was about five. Then, with the process of suppressing the speckle, this number came to about one in the last fixed-point iteration. Suppose that the patch size in the PPB filter is $P \times P$, and the size of the nonlocal searching windows in the PPB and NHANLF methods is $S \times S$. Assuming the calculation of the similarity between two pixels to be one step, then the computational complexity of the PPB filter is about $O(20 \times P^2 \times S^2)$; meanwhile, assuming one Newton iteration of a pixel to be one step, then the average computational complexity of the NHANLF model is about $O(10 \times 3 \times S^2)$. In practice, the processing time of one step of the PPB filter was found to be between two and three times less than that of the NHANLF method, when we tested them in the same programming platform, since both steps only involve a simple numerical computation. Therefore, the NHANLF method is theoretically faster than the PPB filter. The aforementioned analyses imply that, from the aspect of both reducing the speckle and easing the storage and computational load, the proposed NHANLF method could be a good choice when filtering images with a very large size.

C. Choice of the Filtering Parameters

There are three parameters that need to be tuned in the proposed algorithms: the parameter k in (20), the estimation window to calculate LHI in (18), and the scalar parameter h in the weight functions. We found that, for most images, when the value of k is between 200 and 400, the filtering results are quite effective. Therefore, k was fixed as 300 in all of the experiments. For the estimation window to calculate LHI, we found that, in most cases, when this window is set to 3×3 to 7×7, the filtering results are comparable. Therefore, to improve the computation time and storage efficiency, this window was set to 3×3 in the experiments.

For parameter h, since the noise amount of the preprocessed image changes with the process of iteration, we should alter the scalar parameter h in the weight functions of the two proposed models to compensate for the noise accordingly. Therefore, in this study, as in [30], h was obtained by the "noise estimator" proposed by Canny [41]: at the beginning of each fixed-point iteration, the histogram of the absolute values of the similarity between any two neighboring pixels throughout the preprocessed image is computed, and h is set to be approximately the 90% value of the integral.

VI. CONCLUSION

In this paper, we have presented two variational methods for the despeckling of SAR images, which introduce the nonlocal regularization functionals derived for the original and the logarithmic domains of SAR data, respectively. The statistical properties of the speckle and the log-transformed speckle are analyzed, and the similarity measurements between pixels in the homomorphic domain and nonhomomorphic domain are derived to construct the corresponding nonlocal regularization functionals. In the proposed models, we have developed a strategy to adaptively choose the regularization parameters based on both the local heterogeneity information and the noise level of the images, aiming at getting a better balance between the goodness of fit of the original data and the amount of smoothing. The proposed techniques compared favorably with regard to several variational methods in experiments with four physically simulated images and two real SAR images, with good results both in reducing speckle and retaining image details. We also compared the proposed models with other state-of-the-art methods, which again confirmed the competitive performances of the proposed models in processing SAR data. In addition, it was found that the proposed NHANLF model can generally achieve better despeckling results than the HANLF model when the noise level is high.

APPENDIX
EXISTENCE AND UNIQUENESS OF THE SOLUTION OF THE PROPOSED MODELS

1) To simplify the Euler–Lagrange equation of the NHANLF model, let $X = u(x)$ and $W_1 = \exp\{-[\log((v_1(x)+v_1(y))/\sqrt{v_1(x)v_1(y)})/h]^2\}$, and it is then reduced to

$$F_1(X) = \int_\Omega \frac{X-u(y)}{X+u(y)} \cdot \frac{1}{2} W_1 dy + \lambda(x)\left(-\frac{f(x)}{X}+1\right) = 0 \quad (38)$$

and the first-order derivative of the function $F_1(X)$ with respect to X is

$$F_1'(X) = \int_\Omega \frac{u(y)}{[X+u(y)]^2} \times W_1 dy + \frac{\lambda(x) f(x)}{X^2} \quad (39)$$

where $u(y)$, $f(x)$, and $\lambda(x)$ are all positive, so $F_1'(X)$ is also always positive, which means that $F_1(X)$ monotonically increases with X. Meanwhile, it can be proved that, when X is positive and close to 0, $F_1(X) \to -\infty$, and when $X \to +\infty$, $F_1(X) \to \int_\Omega (1/2) W dy + \lambda(x) > 0$. Therefore, we can say that the Euler–Lagrange equation in (38) has only one positive solver X^*. In addition, when $X < X^*$, $F_1(X) < 0$, and the functional J_1 in (15) monotonically decreases; when $X > X^*$, $F_1(X) > 0$, and J_1 monotonically increases. This indicates the uniqueness of the solution of the NHANLF model.

2) Let $W_2 = \exp\{-[(v_2(x) - v_2(y))/h]^2\}$, and the Euler–Lagrange equation of the HANLF model is then reduced to

$$F_2(E(x)) = \int_\Omega 2\left[E(x) - E(y)\right] W_2 dy + \lambda(x)\left[-f(x)e^{-E(x)} + 1\right] = 0. \quad (40)$$

The first-order derivative of the function $F_2(E(x))$ with respect to $E(x)$ $(E(x) \in (-\infty, +\infty))$ is

$$F_2'(E(x)) = \int_\Omega 2W_2 dy + \lambda(x) f(x) e^{-E(x)}. \quad (41)$$

Clearly, $F_2'(E(x))$ is also always positive, which means that $F_2(E(x))$ monotonically increases with $E(x)$. In addition, when $E(x) \to -\infty$, $F_2(E(x)) \to -\infty$, and when $E(x) \to +\infty$, $F_2(E(x)) \to +\infty$. Therefore, we can say that the Euler–Lagrange equation in (40) has only one solver $E^*(x)$, and this solver minimizes the functional J_2.

REFERENCES

[1] J. S. Lee, M. R. Grunes, and G. D. Grandi, “Polarimetric SAR speckle filtering and its implication for classification,” *IEEE Trans. Geosci. Remote Sens.*, vol. 37, no. 5, pp. 2363–2373, Sep. 1999.

[2] X. Ma, H. Shen, J. Yang, L. Zhang, and P. Li, “Polarimetric-spatial classification of SAR images based on the fusion of multiple classifiers,” *IEEE J. Sel. Topics Appl. Earth Observ. Remote Sens.*, vol. 7, no. 3, pp. 961–971, Mar. 2014.

[3] J. S. Lee, “Digital image enhancement and noise filtering by use of local statistics,” *IEEE Trans. Pattern Anal. Mach. Intell.*, vol. PAMI-2, no. 2, pp. 165–168, Mar. 1980.

[4] D. T. Kuan, A. A. Sawchuk, T. C. Strand, and P. Chavel, “Adaptive noise smoothing filter for images with signal-dependent noise,” *IEEE Trans. Pattern Anal. Mach. Intell.*, vol. PAMI-7, no. 2, pp. 165–177, Mar. 1985.

[5] J. S. Lee, “A simple speckle smoothing algorithm for synthetic aperture radar images,” *IEEE Trans. Syst., Man Cybern.*, vol. SMC-13, no. 1, pp. 85–89, Jan./Feb. 1983.

[6] J. S. Lee, “Refined filtering of image noise using local statistics,” *Comput. Graph. Image Process.*, vol. 15, no. 4, pp. 380–389, 1981.

[7] J. S. Lee, J. H. Wen, T. L. Ainsworth, K. S. Chen, and A. J. Chen, “Improved sigma filter for speckle filtering of SAR imagery,” *IEEE Trans. Geosci. Remote Sens.*, vol. 47, no. 1, pp. 202–213, Jan. 2009.

[8] P. F. Yan and C. H. Chen, “An algorithm for filtering multiplicative noise in wide range,” *Traitement du Signal*, vol. 3, no. 2, pp. 91–96, 1986.

[9] H. H. Arsenault and M. Levesque, “Combined homomorphic and local-statistics processing for restoration of images degraded by signal-dependent noise,” *Appl. Opt.*, vol. 23, no. 6, pp. 845–850, Mar. 1984.

[10] C. A. Deledalle, L. Denis, and F. Tupin, “Iterative weighted maximum likelihood denoising with probabilistic patch-based weights,” *IEEE Trans. Image Process.*, vol. 18, no. 12, pp. 2661–2672, Dec. 2009.

[11] Z. Hua, Y. W. Li, and L. C. Jiao, “SAR image despeckling using Bayesian nonlocal means filter with sigma preselection,” *IEEE Geosci. Remote Sens. Lett.*, vol. 8, no. 4, pp. 809–813, Jul. 2011.

[12] T. Teuber and A. Lang, “A new similarity measure for nonlocal filtering in the presence of multiplicative noise,” *Comput. Statist. Data Anal.*, vol. 56, no. 12, pp. 3821–3842, 2012.

[13] C. Deledalle, L. Denis, G. Poggi, F. Tupin, and L. Verdoliva, “Exploiting patch similarity for SAR image processing: The nonlocal paradigm,” *IEEE Signal Process. Mag.*, vol. 31, no. 4, pp. 69–78, Jul. 2014.

[14] S. Parrilli, M. Poderico, C. V. Angelino, and L. Verdoliva, “A nonlocal SAR image denoising algorithm based on LLMMSE wavelet shrinkage,” *IEEE Trans. Geosci. Remote Sens.*, vol. 50, no. 2, pp. 606–616, Feb. 2012.

[15] H. C. Li, W. Hong, Y. R. Wu, and P. Z. Fan, “Bayesian wavelet shrinkage with heterogeneity-adaptive threshold for SAR image despeckling based on generalized gamma distribution,” *IEEE Trans. Geosci. Remote Sens.*, vol. 51, no. 4, pp. 2388–2402, Apr. 2013.

[16] F. Argenti, T. Bianchi, A. Lapini, and L. Alparone, “Fast MAP despeckling based on Laplacian–Gaussian modeling of wavelet coefficients,” *IEEE Geosci. Remote Sens. Lett.*, vol. 9, no. 1, pp. 13–17, Jan. 2012.

[17] F. Argenti, A. Lapini, L. Alparone, and T. Bianchi, “A tutorial on speckle reduction in synthetic aperture radar images,” *IEEE Geosci. Remote Sens. Mag.*, vol. 1, no. 3, pp. 6–35, Sep. 2013.

[18] X. Ma, H. Shen, L. Zhang, J. Yang, and H. Zhang, “Adaptive anisotropic diffusion method for polarimetric SAR speckle filtering,” *IEEE J. Sel. Topics Appl. Earth Observ. Remote Sens.*, vol. 8, no. 3, pp. 1041–1050, Mar. 2015.

[19] L. I. Rudin, S. Osher, and E. Fatemi, “Nonlinear total variation based noise removal algorithms,” *Physica D, Nonlinear Phenomena*, vol. 60, no. 1, pp. 259–268, 1992.

[20] H. Shen, L. Peng, L. Yue, Q. Yuan, and L. Zhang, “Adaptive norm selection for regularized image restoration and super-resolution,” *IEEE Trans. Cybern.*, to be published.

[21] Q. Yuan, L. Zhang, and H. Shen, “Hyperspectral image denoising employing a spectral–spatial adaptive total variation model,” *IEEE Trans. Geosci. Remote Sens.*, vol. 50, no. 10, pp. 3660–3677, Oct. 2012.

[22] G. Aubert and J. F. Aujol, “A variational approach to removing multiplicative noise,” *SIAM J. Appl. Math.*, vol. 68, no. 4, pp. 925–946, 2008.

[23] J. N. Shi and S. Osher, “A nonlinear inverse scale space method for a convex multiplicative noise model,” *SIAM J. Imaging Sci.*, vol. 1, no. 3, pp. 294–321, 2008.

[24] Y. M. Huang, M. K. Ng, and Y. W. Wen, “A new total variation method for multiplicative noise removal,” *SIAM J. Imaging Sci.*, vol. 2, no. 1, pp. 20–40, 2009.

[25] G. Steidl and T. Teuber, “Removing multiplicative noise by Douglas–Rachford splitting methods,” *J. Math. Imaging Vis.*, vol. 36, no. 2, pp. 168–184, 2010.

[26] T. Teuber, G. Steidl, and R. H. Chan, "Minimization and parameter estimation for seminorm regularization models with I-divergence constraints," *Inv. Probl.*, vol. 29, no. 3, pp. 1–33, 2013.

[27] S. Yun and H. Woo, "A new multiplicative denoising variational model based on mth root transformation," *IEEE Trans. Image Process.*, vol. 21, no. 5, pp. 2523–2533, May 2012.

[28] X. L. Zhao, F. Wang, and M. K. Ng, "A new convex optimization model for multiplicative noise and blur removal," *SIAM J. Imaging Sci.*, vol. 7, no. 1, pp. 456–475, 2014.

[29] G. Gilboa and S. Osher, "Nonlocal operators with applications to image processing," *Multiscale Model. Simul.*, vol. 7, no. 3, pp. 1005–1028, 2008.

[30] Y. Lou, X. Zhang, S. Osher, and A. Bertozzi, "Image recovery via nonlocal operators," *J. Sci. Comput.*, vol. 42, no. 2, pp. 185–197, 2010.

[31] A. Buades, B. Coll, and J. M. Morel, "A non-local algorithm for image denoising," in *Proc. IEEE Comput. Soc. Conf. CVPR*, 2005, vol. 2, pp. 60–65.

[32] G. Chierchia, N. Pustelnik, B. Pesquet-Popescu, and J. Pesquet, "A non-local structure tensor-based approach for multicomponent image recovery problems," *IEEE Trans. Image Process.*, vol. 23, no. 12, pp. 5531–5544, Dec. 2014.

[33] H. Xie, L. E. Pierce, and F. T. Ulaby, "Statistical properties of logarithmically transformed speckle," *IEEE Trans. Geosci. Remote Sens.*, vol. 40, no. 3, pp. 721–727, Mar. 2002.

[34] L. Fang, M. K. Ng, and C. M. Shen, "Multiplicative noise removal with spatially varying regularization parameters," *SIAM J. Imaging Sci.*, vol. 3, no. 1, pp. 1–20, 2010.

[35] D. Chen and L. Cheng, "Spatially adapted total variation model to remove multiplicative noise," *IEEE Trans. Image Process.*, vol. 21, no. 4, pp. 1650–1662, Apr. 2012.

[36] Ortega, M. James, and W. C. Rheinboldt, *Iterative Solution of Nonlinear Equations in Several Variables*, vol. 30. Philadelphia, PA, USA: SIAM, 2000.

[37] S. Kindermann, S. Osher, and P. W. Jones, "Deblurring and denoising of images by nonlocal functionals," *Multiscale Model. Simul.*, vol. 4, no. 4, pp. 1091–1115, 2005.

[38] G. D. Martino, M. Poderico, G. Poggi, D. Riccio, and L. Verdoliva, "Benchmarking framework for SAR despeckling," *IEEE Trans. Geosci. Remote Sens.*, vol. 52, no. 3, pp. 1596–1615, Mar. 2014.

[39] G. Franceschetti, M. Migliaccio, D. Riccio, and G. Schirinzi, "SARAS: A SAR raw signal simulator," *IEEE Trans. Geosci. Remote Sens.*, vol. 30, no. 1, pp. 110–123, Jan. 1992.

[40] W. K. Pratt, *Digital Image Processing*. New York, NY, USA: Interscience, 1978.

[41] J. Canny, "A computational approach to edge detection," *IEEE Trans. Pattern Anal. Mach. Intell.*, vol. PAMI-8, no. 6, pp. 679–698, Nov. 1986.

Xiaoshuang Ma received the B.S. degree in geographic information system from Hubei University, Wuhan, China, in 2011. He is currently working toward the Ph.D. degree in the School of Resource and Environmental Sciences, Wuhan University, Wuhan.

His research interests include synthetic aperture radar (SAR) image interpretation (segmentation and classification) and SAR signal processing.

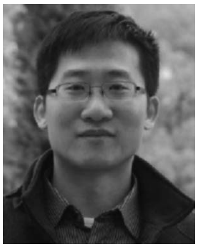

Huanfeng Shen (M'10–SM'13) received the B.S. degree in surveying and mapping engineering and the Ph.D. degree in photogrammetry and remote sensing from Wuhan University, Wuhan, China, in 2002 and 2007, respectively.

In July 2007, he joined the School of Resource and Environmental Sciences, Wuhan University, where he is currently a Luojia Distinguished Professor. He has been supported by several talent programs, such as The Youth Talent Support Program of China (2015), China National Science Fund for Excellent Young Scholars (2014), and the New Century Excellent Talents by the Ministry of Education of China (2011). He is currently a member of the Editorial Board of the *Journal of Applied Remote Sensing*. He has published more than 100 research papers. His research interests include image quality improvement, remote sensing mapping and application, data fusion and assimilation, and regional and global environmental change.

Xile Zhao received the M.S. and Ph.D. degrees from the University of Electronic Science and Technology of China (UESTC), Chengdu, China, in 2009 and 2012, respectively.

He is currently an Associate Professor with the School of Mathematical Sciences, UESTC. His main research interests are sparse and low-rank modeling for high-dimensional data analysis.

Liangpei Zhang (M'06–SM'08) received the B.S. degree in physics from Hunan Normal University, Changsha, China, in 1982, the M.S. degree in optics from Xi'an Institute of Optics and Precision Mechanics, Chinese Academy of Sciences, Xi'an, China, in 1988, and the Ph.D. degree in photogrammetry and remote sensing from Wuhan University, Wuhan, China, in 1998.

He is currently the Head of the Remote Sensing Division, State Key Laboratory of Information Engineering in Surveying, Mapping, and Remote Sensing (LIESMARS), Wuhan University. He is also a Chang-Jiang Scholar Chair Professor appointed by the Ministry of Education of China. He is currently a Principal Scientist for the China State Key Basic Research Project (2011–2016) appointed by the Ministry of National Science and Technology of China to lead the remote sensing program in China. He has more than 450 research papers and five books. He is the holder of 15 patents. His research interests include hyperspectral remote sensing, high-resolution remote sensing, image processing, and artificial intelligence.

Dr. Zhang is the Founding Chair of the IEEE Geoscience and Remote Sensing Society (GRSS) Wuhan Chapter. He is a Fellow of the Institution of Engineering and Technology (IET), an executive member (Board of Governor) of the China National Committee of International Geosphere–Biosphere Programme, an executive member of the China Society of Image and Graphics, etc. He was a recipient of the 2010 Best Paper Boeing Award and the 2013 Best Paper ERDAS Award from the American Society of Photogrammetry and Remote Sensing (ASPRS). He received the Best Reviewer Awards from the IEEE GRSS for his service to the IEEE JOURNAL OF SELECTED TOPICS IN EARTH OBSERVATIONS AND APPLIED REMOTE SENSING (JSTARS) in 2012 and IEEE GEOSCIENCE AND REMOTE SENSING LETTERS (GRSL) in 2014. He was the General Chair of the 4th IEEE GRSS Workshop on Hyperspectral Image and Signal Processing: Evolution in Remote Sensing (WHISPERS) and the Guest Editor of JSTARS. His research teams won the top three prizes of the IEEE GRSS 2014 Data Fusion Contest, and his students have been selected as the winners or finalists of the IEEE International Geoscience and Remote Sensing Symposium (IGARSS) student paper contest in recent years. He regularly serves as a Cochair of the series SPIE Conferences on Multispectral Image Processing and Pattern Recognition, Conference on Asia Remote Sensing, and many other conferences. He edits several conference proceedings, issues, and geoinformatics symposiums. He also serves as an Associate Editor of the *International Journal of Ambient Computing and Intelligence*, *International Journal of Image and Graphics*, *International Journal of Digital Multimedia Broadcasting*, *Journal of Geo-spatial Information Science*, and *Journal of Remote Sensing*, and the Guest Editor of the *Journal of Applied Remote Sensing* and *Journal of Sensors*. He is currently serving as an Associate Editor of the IEEE TRANSACTIONS ON GEOSCIENCE AND REMOTE SENSING.